



Numerical noise prediction and source identification of a realistic landing gear

Tulio R. Ricciardi
William R. Wolf

University of Campinas, Brazil
tulioricci@fem.unicamp.br

Nicholas J. Moffitt
Jordan R. Kreitzman
Paul Bent

Boeing Research & Technology

AMS Seminar, 2021/05/27

Airplane acoustics

- Aeroacoustics:
  - Unsteady flows create pressure disturbances (acoustic waves)
  - Motivated by (loud) jet-powered aircraft after WW2
- More efficient turbo-fan engines are quieter
- The contribution from solid surfaces becomes more important (fluid-structure interaction)
- Airframe noise
  - High-lift devices
  - Main and nose landing gears
  - Parasitic noise (vents, cavities, holes, etc)

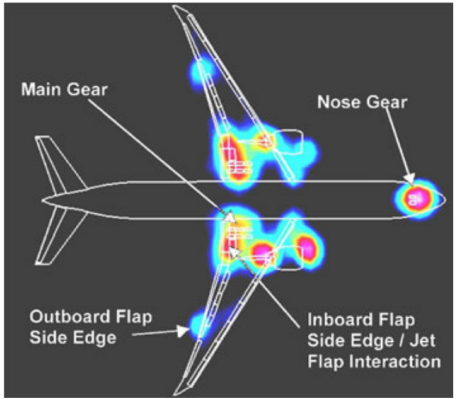
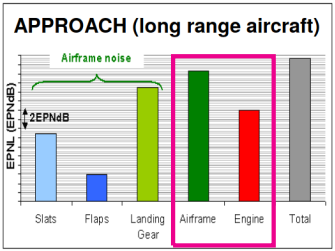


Fig. 1: Identification of noise sources using beamforming technique **[1]**.

[1] Langtry et al. Flow, Turbulence and Combustion, October 2013, Volume 91, Issue 3

Airframe noise

- Airframe noise sources are dominant in approach conditions (landing)
  - Idle engine, with low noise emission
  - High-lift devices + main & nose landing gears are fully deployed
  - Flow interaction between exposed components



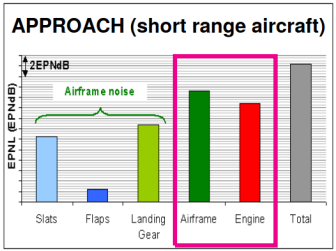


Fig. 2: Noise contribution in approach condition **[2]**.



Fig. 3: B747 main landing gear and high-lift devices.

[2] Dobrzynski, W. Journal of Aircraft, 2010, Volume 47, No 2

Landing gear noise

- Assembly of multiple blunt bodies and cavities
  - Complex fluid-structure interaction
  - Broadband noise due to turbulent flow separation
  - Tonal peaks may appear due to cavity resonances
- Experiments are limited to small-scale models due to size limitations of wind tunnels:
  - Different conditions (geometry and flow)
  - Benefits (and challenges) of numerical simulations
- Landing gears are critical components: several constraints in terms of weight, cost, safety, aerodynamic and structural requirements, etc
  - Understand the physics to avoid trial-and-error



Fig. 4: Landing gear studied in this work.

Landing gear noise

- Assembly of multiple blunt bodies and cavities
  - Complex fluid-structure interaction
  - Broadband noise due to turbulent flow separation
  - Tonal peaks may appear due to cavity resonances
- Experiments are limited to small-scale models due to size limitations of wind tunnels:
  - Different conditions (geometry and flow)
  - Benefits (and challenges) of numerical simulations
- Landing gears are critical components: several constraints in terms of weight, cost, safety, aerodynamic and structural requirements, etc
  - Understand the physics to avoid trial-and-error



Fig. 4: Scale model at 26% of the 777 main landing gear (note the absence of cavity) **[3]**.

[3] Jaeger et al, AIAA 2002-2410

Landing gear noise

- Assembly of multiple blunt bodies and cavities
  - Complex fluid-structure interaction
  - Broadband noise due to turbulent flow separation
  - Tonal peaks may appear due to cavity resonances
- Experiments are limited to small-scale models due to size limitations of wind tunnels:
  - Different conditions (geometry and flow)
  - Benefits (and challenges) of numerical simulations
- Landing gears are critical components: several constraints in terms of weight, cost, **safety**, aerodynamic and **structural requirements**, etc
  - Understand the physics to avoid trial-and-error



Fig. 4: Landing gear is a critical component.

Objectives

- Noise prediction from a full-scale realistic nose landing gear
  - CFD solves the hydrodynamic near-field
  - Acoustic analogy is used for far-field noise prediction
- Compare a full complexity geometry and its partially simplified version
  - Simplified geometry is cheaper: fewer surface and BL cells
  - Is a simplified geometry cost effective? Is it trustworthy for design purposes?
  - What is the influence of small components? Are they necessary?
- Post-processing of unsteady data to identify noise sources
  - Not only predict, but understand the physics
  - Proper orthogonal decomposition
  - Analysis of cavity modes

Objectives

- Noise prediction from a full-scale realistic nose landing gear
  - CFD solves the hydrodynamic near-field
  - Acoustic analogy is used for far-field noise prediction
- Compare a full complexity geometry and its partially simplified version
  - Simplified geometry is cheaper: fewer surface and BL cells
  - Is a simplified geometry cost effective? Is it trustworthy for design purposes?
  - What is the influence of small components? Are they necessary?
- Post-processing of unsteady data to identify noise sources
  - Not only predict, but understand the physics
  - Proper orthogonal decomposition
  - Analysis of cavity modes

Objectives

- Noise prediction from a full-scale realistic nose landing gear
  - CFD solves the hydrodynamic near-field
  - Acoustic analogy is used for far-field noise prediction
- Compare a full complexity geometry and its partially simplified version
  - Simplified geometry is cheaper: fewer surface and BL cells
  - Is a simplified geometry cost effective? Is it trustworthy for design purposes?
  - What is the influence of small components? Are they necessary?
- Post-processing of unsteady data to identify noise sources
  - Not only predict, but understand the physics
  - Proper orthogonal decomposition
  - Analysis of cavity modes

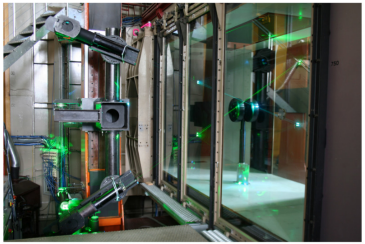
Numerical methodology

- Boeing's BCFD in-house code **[4]**
- Delayed detached eddy simulation:
  - Class of Wall-Modeled LES
- Finite volume method 2^{nd} order: upwind+centered scheme **[5]**
- Inviscid flux: HLLE scheme
- Dual time stepping for stable and accurate large physical time steps:
  - CFL $\approx$ 700 in BL
  - CFL $\approx$ 1 in the wake
- Ffowcs-Williams and Hawkings acoustic analogy (frequency domain **[6]**)
  - Solid and permeable FWH surface
- Numerical tools and methodology validated for the LAGOON model landing gear:
  - Numerical and experimental database from the BANC workshop

[4] Cary et al, AIAA 2009-3650
[5] Winkler et al, AIAA 2012-0570
[6] Lockard, AIAA 2002-2580

LAGOON

- Simplified 40% scale geometry from Airbus A320 (main strut, wheels, cavity, axle)
- AIAA BANC Workshop
- Results for velocity fields, noise, steady and unsteady surface pressure



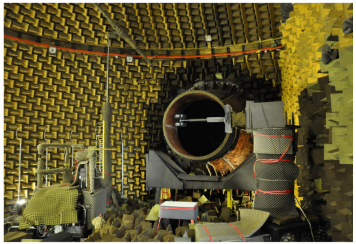


Fig. 5: Experiments performed by ONERA **[7,8]**.

- Mach number $= 0.23$
- Reynolds number $Re_D \approx 1.5 \times 10^6$
- 100M grid points

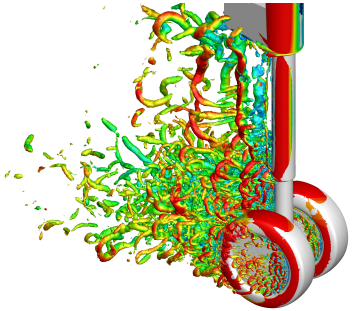


Fig. 6: Multiple length-scales in turbulent flow separation.

[7,8] Manoha et al, AIAA 2008-2816 and 2009-3277

Velocity field

- Good agreement in terms of mean and RMS velocity field
- Closed wind-tunnel x unbounded simulation

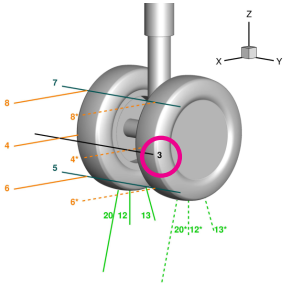


Fig. 8: Reference locations for velocity comparisons.

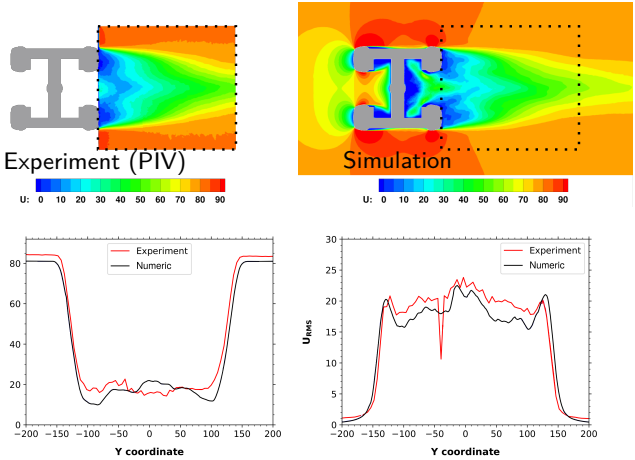


Fig. 7: Comparison of numerical and experimental in terms of velocity field for streamwise component.

Surface pressure intermittency

- Unsteady pressure on the surface (solid FWH)
- Good agreement for mid-frequencies and tones

Red and **green**: experiments

Black and **gray**: numerical (symmetry)

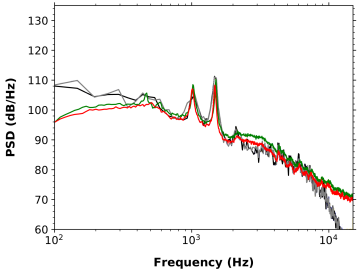


Fig. 9: Fourier spectra on the wheel surface, upstream of the cavity (K15).

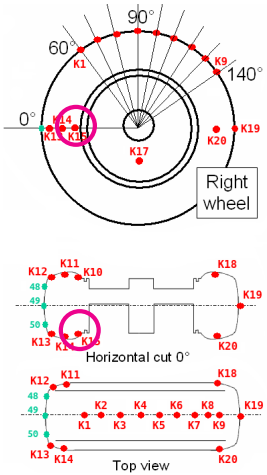


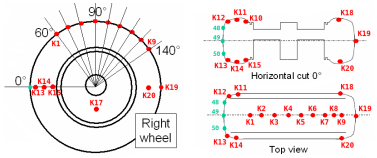
Fig. 10: Probe locations.

Surface pressure intermittency

- Unsteady pressure on the surface (solid FWH)
- Good agreement for mid-frequencies and tones
- Time-frequency analysis using wavelet transform

Red and **green**: experiments

Black and **gray**: numerical (symmetry)



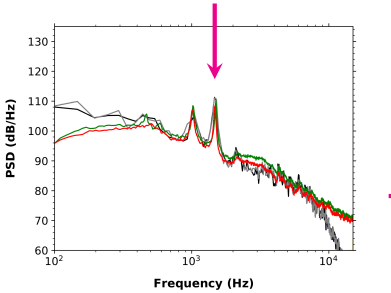


Fig. 9: Fourier spectra on the wheel surface, upstream of the cavity (K15).

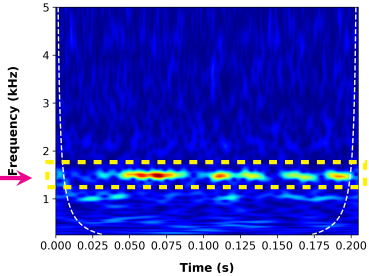


Fig. 10: Wavelet transform presents intermittency in the signal.

Surface pressure intermittency

- Unsteady pressure on the surface (solid FWH)
- Good agreement for mid-frequencies and tones
- Time-frequency analysis using wavelet transform
- Intermittency and noise emission

Green: loud

Red and **blue**: quiet

Black: averaged noise

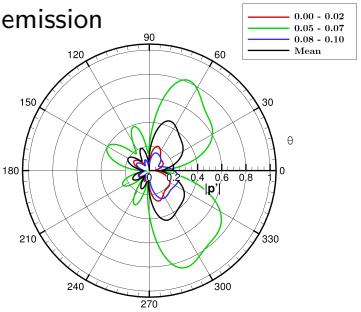


Fig. 9: Noise directivity at 1.5kHz for different time instants.

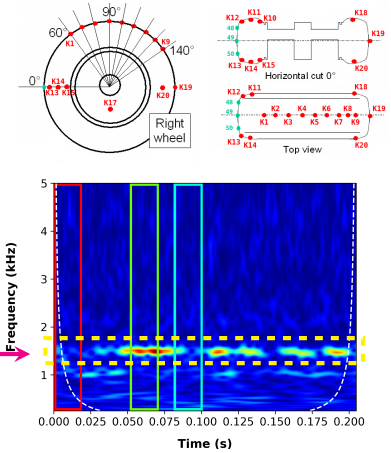


Fig. 10: Wavelet transform presents intermittency in the signal.

Noise prediction

- Good agreement between numerical simulations and experiments
- Solid FWH surface only

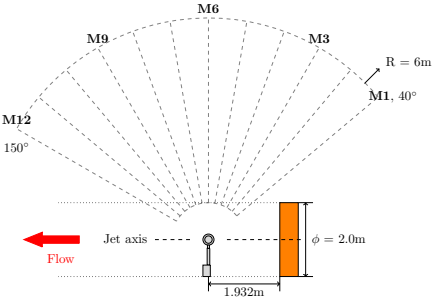


Fig. 11: Microphone location for noise prediction.

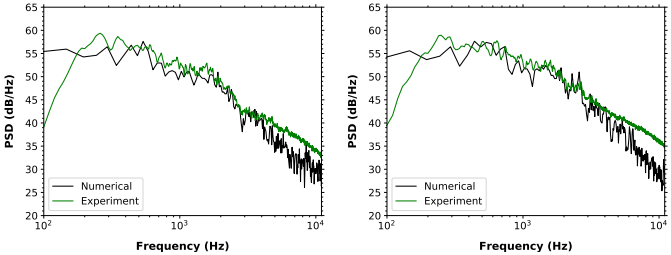


Fig. 12: Comparison of numerical and experimental results for flyover microphones (M6 and M9).

Noise prediction

- Good agreement between numerical simulations and experiments
- Solid FWH surface only
- The black and grey lines are used to verify symmetry in numerical results.

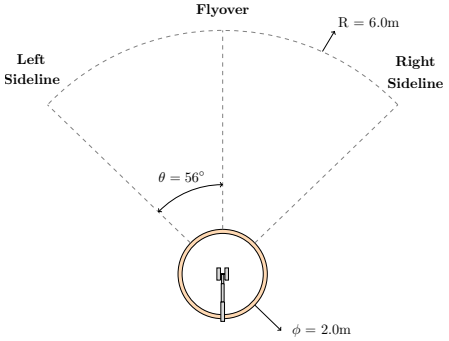


Fig. 13: Microphone location for noise prediction.

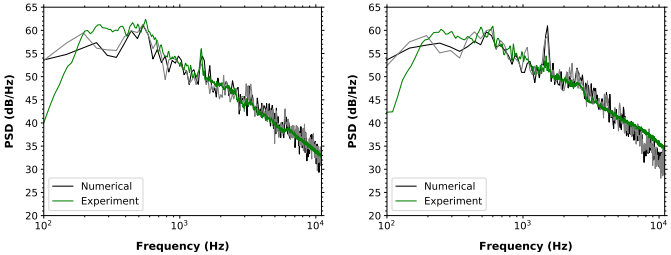


Fig. 14: Comparison of numerical and experimental results for sideline microphones (M6 and M9).

Realistic landing gear

- Numerical simulation as a predictive tool for design and certification of airplanes
- Fly-over conditions (different than landing)
  - Angle of attack $\alpha = 6$ deg.
  - Freestream Mach number 0.3
  - Reynolds number (wheel) $\approx 8.5 \times 10^6$
  - Reynolds number (strut) $\approx 1.5 \times 10^6$
- No experimental data available for full-scale setup
- First simulation was limited to 200M cells
  - guided the simplification process
- Ricciardi et al, Journal of Sound and Vibration 2021, Volume 496

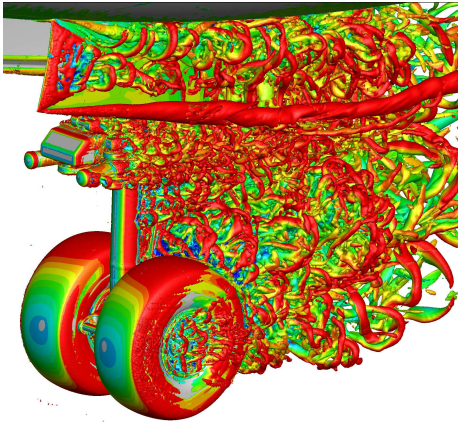
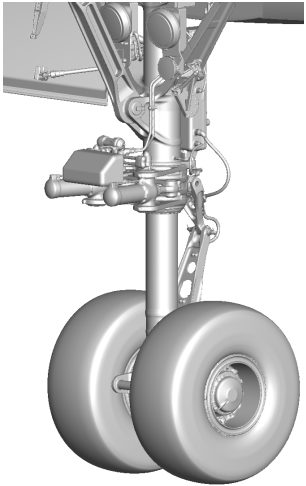


Fig. 15: Iso-surfaces of Q-criterion for current configuration.

Realistic landing gear

- Full-complexity setup retains all features
- The simplified geometry has the main features of the full complexity setup (mid and large-scale components)
- Small-scale components were removed for computational savings
  - Nuts, bolts, lines, supports
  - Fewer surface and BL cells
  - Easier and faster mesh generation



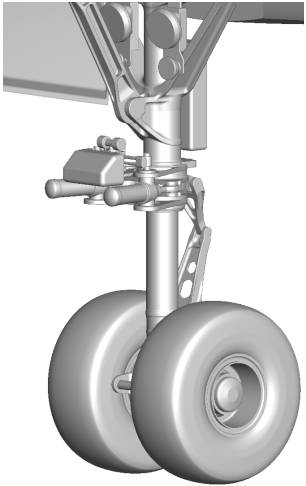


Fig. 16: Full complexity setup. Fig. 17: Simplified setup.

Realistic landing gear

- Full-complexity setup retains all features
- Components inside the cavity were removed (low-speed flow)
- Simplified setup focus on the landing gear itself (exposed to the high-speed flow)

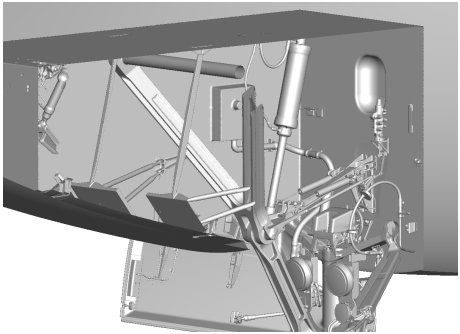


Fig. 18: Full complexity setup.

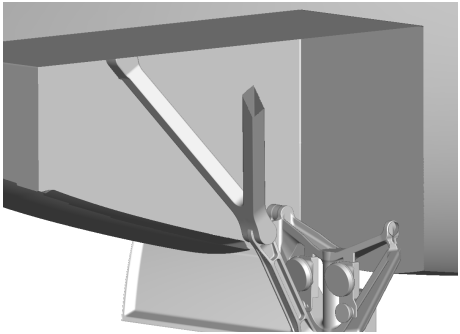


Fig. 19: Simplified setup.

Realistic landing gear

- Different aircraft setups
  - Computational savings
  - Velocity gradient effects

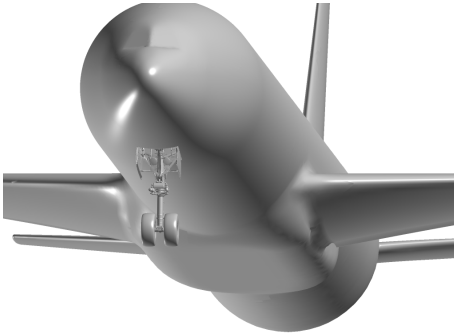


Fig. 20: Full aircraft.

- Full complexity: freestream condition
- Simplified setup: outflow condition

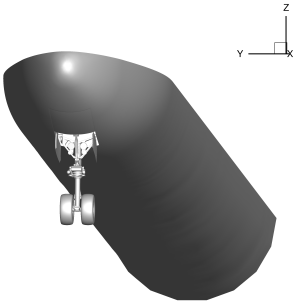


Fig. 21: Simplified aircraft.

Simulation setup

- Convective time unit (CTU) based on freestream velocity and wheel diameter
- *Simp 1* has coarser mesh, preliminary analysis
- *Simp 2* has improved mesh compared to *Simp 1*
- Full complexity have similar cell size to *Simp 2*

Simulation	**Simp 1**	**Simp 2**	**Full**
	UNICAMP		Boeing
Configuration	Simplified LG Simplified aircraft		Full LG Full aircraft
Cell count	175M	465M	1600M
Time step (CTU)	1.05×10^{-3}	1.05×10^{-3}	1.98×10^{-3}
Frequency cut-off (St) solid surf.	9.35	17.00	14.85
Data acquisition period (CTU)	21.5	24.1	34.9
Total CPU cost (hours)	2M	7.5M	8.5M

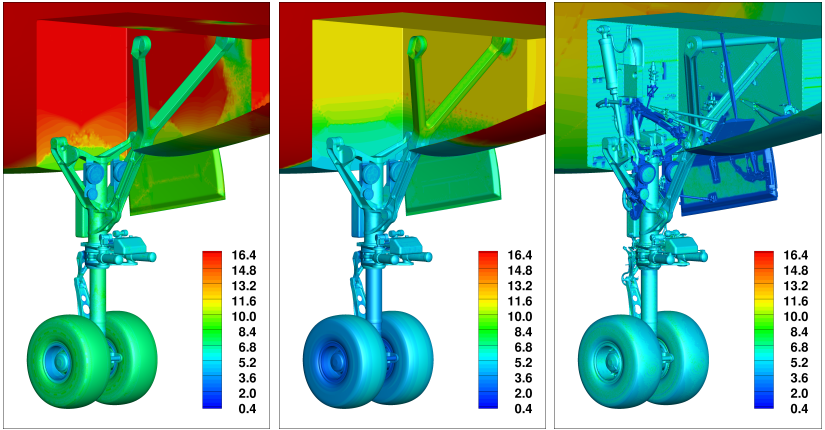
Surface grid

Simplified:

- Coarser cavity
- Localized refinement: small components wheel's cavities corners and edges

Full:

- Automatic generation
- More uniform mesh

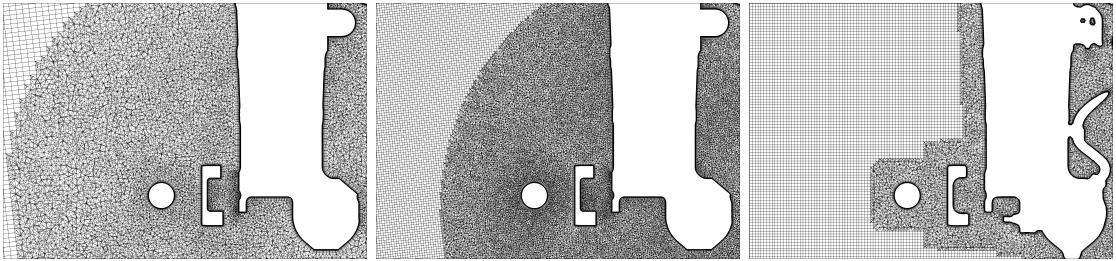


(a) Simp 1 $\approx 100\Delta/D$ (b) Simp 2 $\approx 200\Delta/D$ (c) Full $\approx 175\Delta/D$

Fig. 22: Surface mesh resolution $\Delta/D \times 10^3$, ($\Delta = \sqrt[2]{Area}$).

Volume grid

- Cartesian mesh composed of orthogonal hexahedra has better numerical properties
- Reduced cell count for the same grid resolution ($\Delta = \sqrt[3]{Volume}$)
- Hole-cutting procedure
- Tetrahedra cells fill the region between the boundary layer cells and the hexahedra

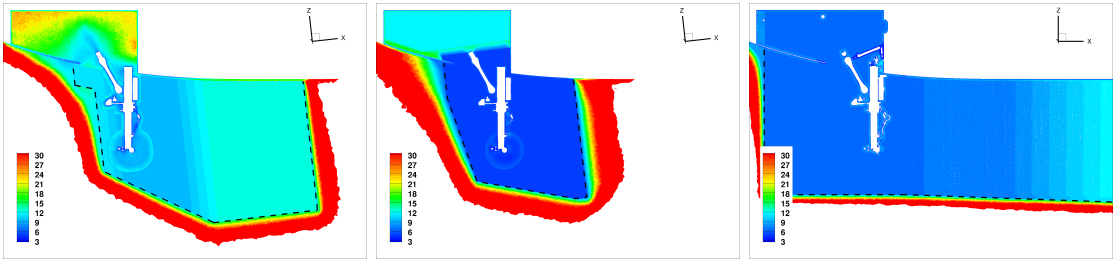


(a) Simp 1 (b) Simp 2 (c) Full

Fig. 23: Hole-cutting procedure for Cartesian mesh.

Volume grid

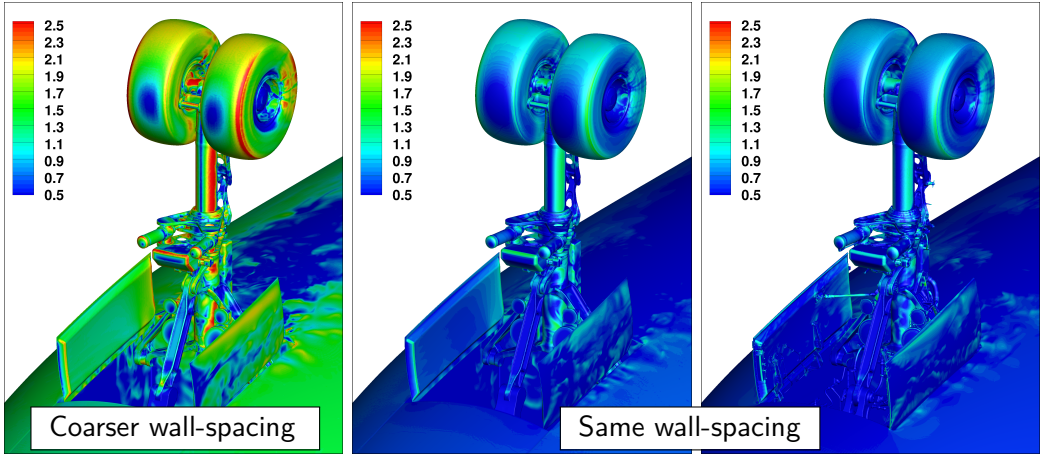
- Simp 1 and 2 transition faster to tets (dashed line) and have coarser cells inside the cavity
- Full complexity setup presents larger Cartesian region, including the cavity
- The permeable FWH surface is placed at the hex-tet transition



(a) Simp 1 (b) Simp 2 (c) Full

Fig. 24: Characteristic length scale $\Delta/D \times 10^3$ for volumetric mesh ($\Delta = \sqrt[3]{Volume}$).

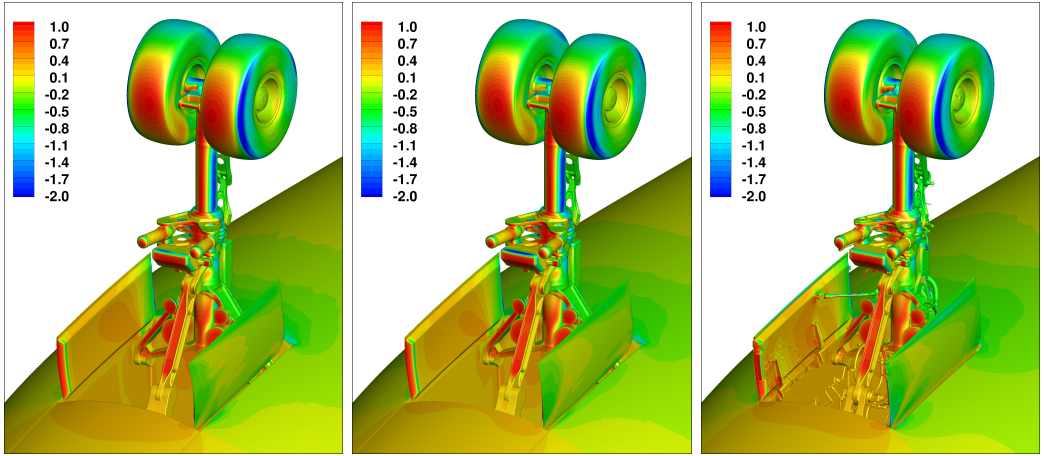
Wall-resolution



(a) Simp 1 (b) Simp 2 (c) Full

Fig. 25: Wall-resolution in terms of Δn^+.

Surface pressure



(a) Simp 1 (b) Simp 2 (c) Full

Fig. 26: Pressure coefficient on LG surface.

Mean velocity fields

- Main differences are consequence of cavity simplification

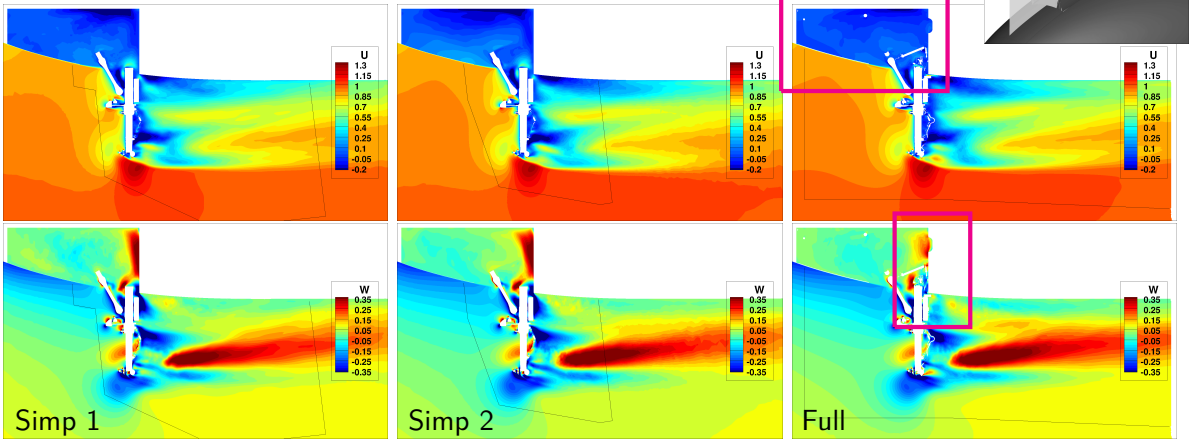


Fig. 27: Mean velocity field at the plane $y = 0$ for U (horizontal) and W (vertical) components.

RMS velocity field

- Main differences are consequence of cavity simplification

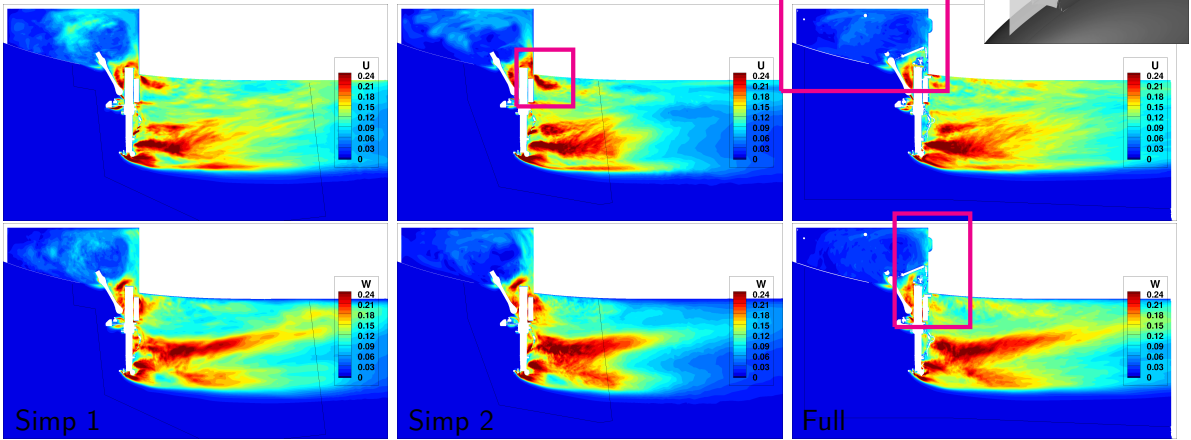


Fig. 28: Unsteady velocity field at the plane $y = 0$ for U (horizontal) and W (vertical) components.

Unsteady surface pressure

Mesh resolution
$\Delta/D \times 10^3$

Unsteady pressure
P_{RMS}

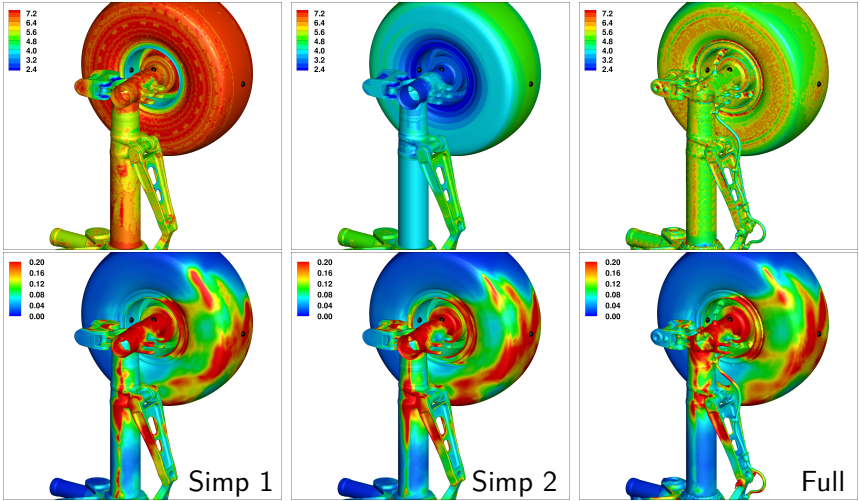


Fig. 29: Mesh resolution and unsteady wall pressure in the wheel-axle region.

Unsteady surface pressure

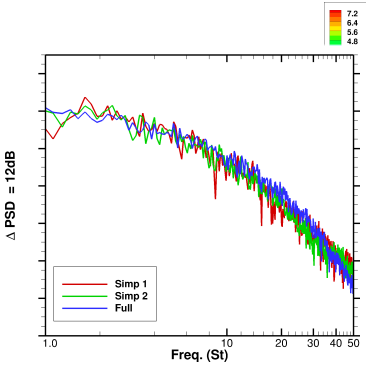


Fig. 30: Wall pressure spectra at the wheel.

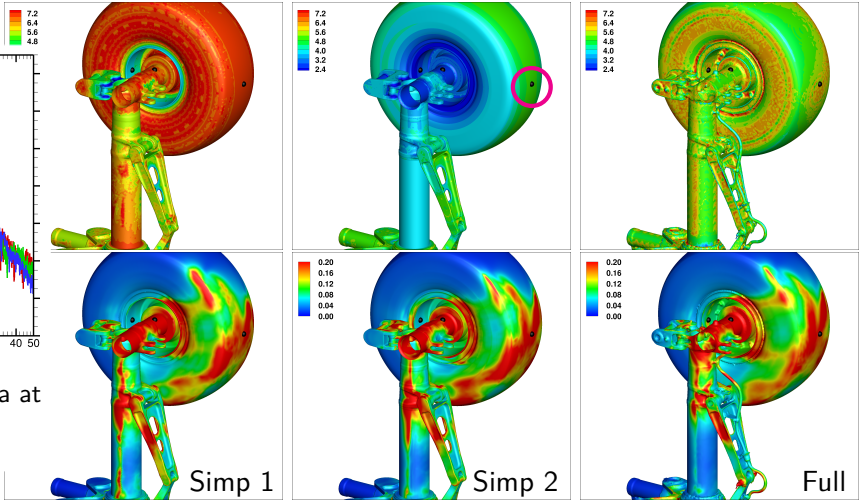


Fig. 29: Mesh resolution and unsteady wall pressure in the wheel-axle region.

Unsteady surface pressure

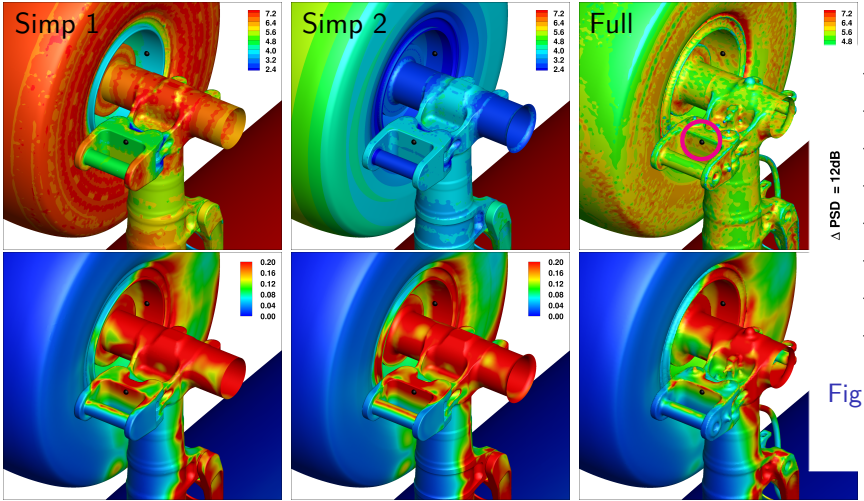


Fig. 31: Mesh resolution and unsteady wall pressure in the wheel-axle region.

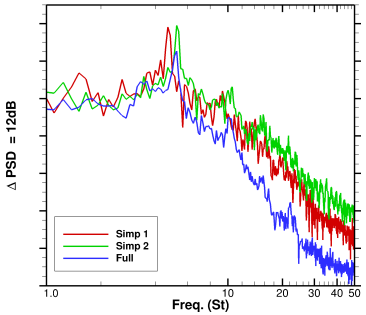


Fig. 32: Wall pressure spectra at the towing link.

Unsteady surface pressure

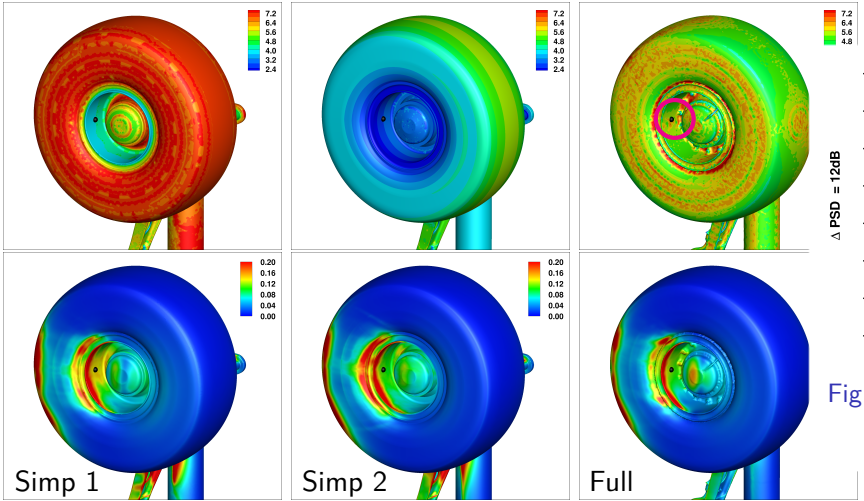


Fig. 33: Mesh resolution and unsteady wall pressure in the wheel external side.

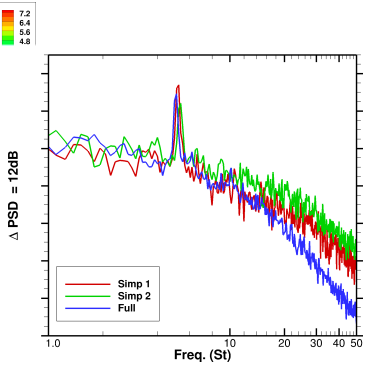


Fig. 34: Wall pressure spectra at the external cavity.

Unsteady surface pressure

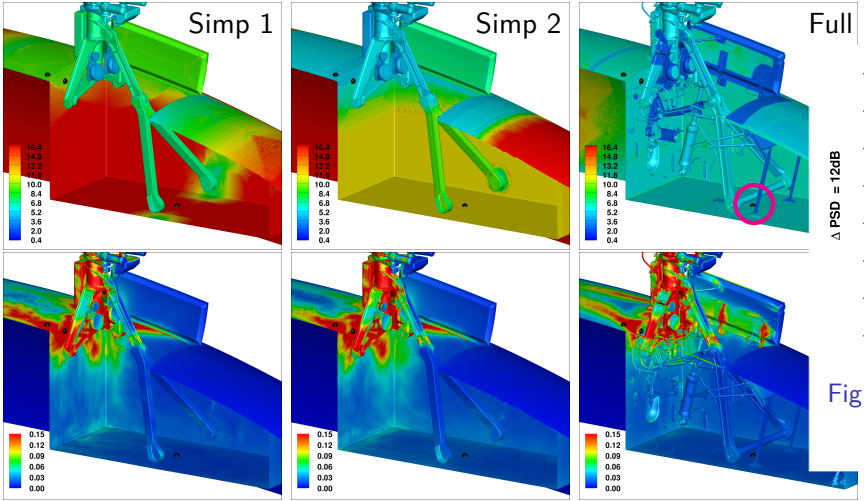


Fig. 35: Mesh resolution and unsteady wall pressure in the fuselage cavity.

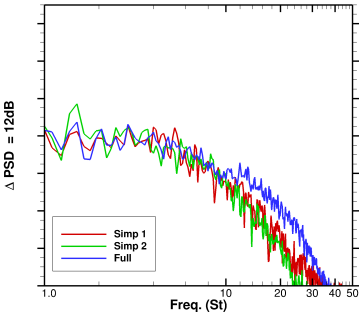


Fig. 36: Wall pressure spectra at the cavity floor.

Unsteady surface pressure

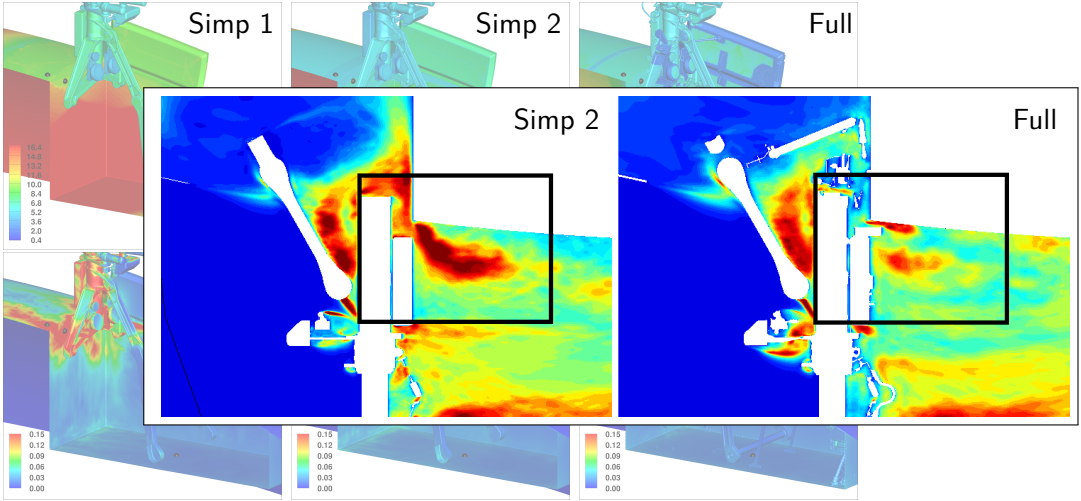


Fig. 35: Mesh resolution and unsteady wall pressure in the fuselage cavity.

Unsteady surface pressure

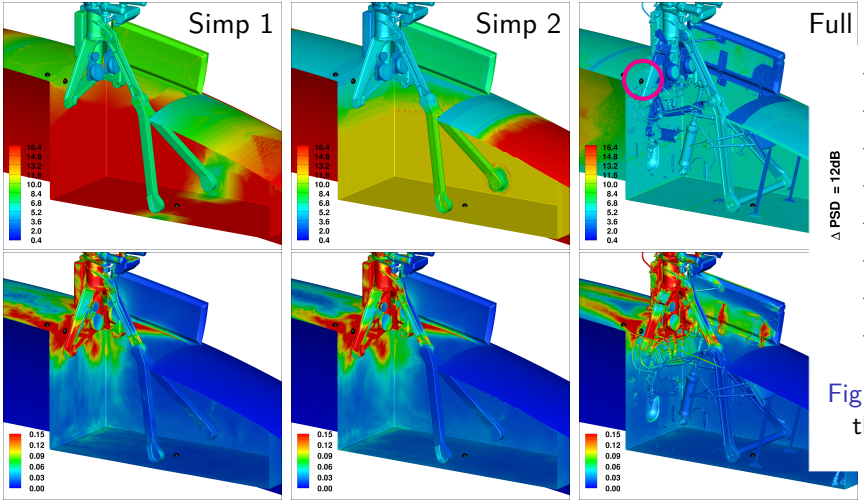


Fig. 35: Mesh resolution and unsteady wall pressure in the fuselage cavity.

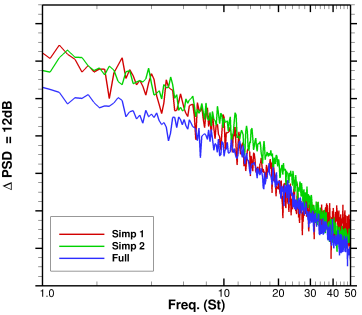


Fig. 36: Wall pressure spectra at the cavity downstream wall.

Unsteady surface pressure

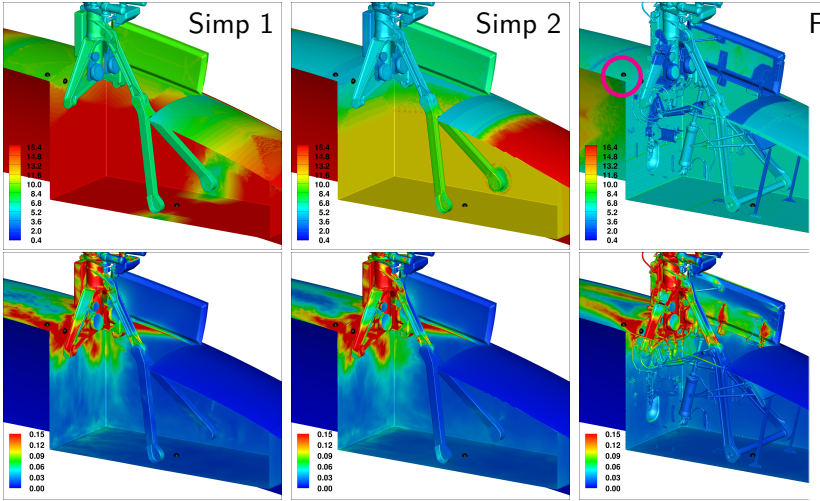


Fig. 35: Mesh resolution and unsteady wall pressure in the fuselage cavity.

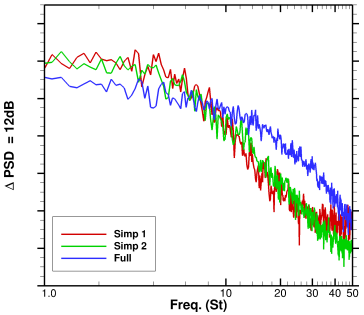


Fig. 36: Wall pressure spectra at the fuselage (downstream of the cavity).

Far-field noise

- Flyover and sideline observers at 90D
- Promising agreement and similar trends for simplified x full complexity
- Simp 1 has earlier frequency cut-off
- Simp 2 and Full have similar levels up to St 20 (close to the design cut-off)

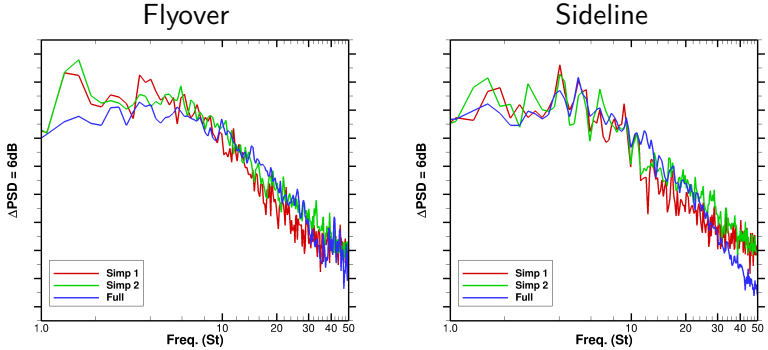


Fig. 37: Far-field noise prediction using solid FWH surface.

Far-field noise - trends by group of components

- Partial integration of solid FWH surface
  - Mathematically, it is not formally precise because a closed surface f is required to satisfy the Heaviside function $H(f)$:

$$\hat{p}'(\mathbf{x})\, H(f) = -\int_{f=0} \left[\hat{F}_i(\mathbf{y}) \frac{\partial G_c(\mathbf{x}, \mathbf{y})}{\partial y_i} \right] dS$$

$$H(f) = \begin{cases} 0, & \text{if } f < 0. \\ 1, & \text{otherwise.} \end{cases}$$

  - The formulation also accounts for acoustic reflections, so one surface may account for noise generated by another.
  - The main idea in this assessment is a purely qualitative analysis focused on **trends** of surface integrated pressure fluctuations.

Far-field noise - trends by group of components

- Mesh refinement effects
  - *Simp 2* has finer mesh
  - *Simp 1* has a mesh finer than *Full* in the axle and wheel's cavities

(1) Axle + Wheel cavities + Tire + Towing link
(2) Fuselage + Cavity + Doors
(3) Strut + Brace + Torque + Steering + Lights

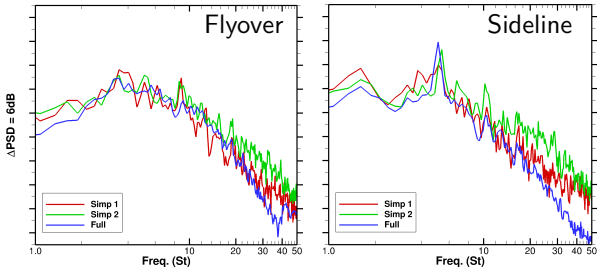


Fig. 38: Far-field noise by partial integration on solid FWH surface.

Far-field noise - trends by group of components

- Mesh refinement effects
  - *Simp 2* has finer mesh
  - *Simp 1* has a mesh finer than *Full* in the axle and wheel's cavities
- Simplification effects
  - *Full* presents lower noise levels at low-frequencies and higher levels at high-frequencies
  - Similar levels for *Simp 1* and *2*

(1) Axle + Wheel cavities + Tire + Towing link
(2) Fuselage + Cavity + Doors
(3) Strut + Brace + Torque + Steering + Lights

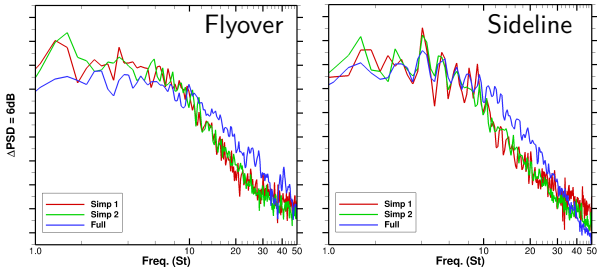


Fig. 38: Far-field noise by partial integration on solid FWH surface.

Far-field noise - trends by group of components

- Mesh refinement effects
  - *Simp 2* has finer mesh
  - *Simp 1* has a mesh finer than *Full* in the axle and wheel's cavities
- Simplification effects
  - *Full* presents lower noise levels at low-frequencies and higher levels at high-frequencies
  - Similar levels for *Simp 1* and *2*
- Simplification + mesh + reflection
  - Noise reflection from the cavity?
  - Small scale components in *Full*
  - *Simp 2* is finer than *Simp 1*, but they present similar levels

(1) Axle + Wheel cavities + Tire + Towing link
(2) Fuselage + Cavity + Doors
(3) Strut + Brace + Torque + Steering + Lights

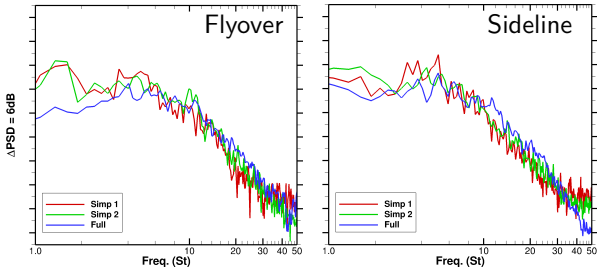


Fig. 38: Far-field noise by partial integration on solid FWH surface.

Geometry comparison

Conclusions of simplification process

- The boundary conditions (half x full fuselage) do not seem to interfere in results.
- Removing the components inside the cavity changed the flow topology:
  - The flow is not so steady as previously thought
  - Blockage effects
  - Components break the large flow structures in small scale turbulence
  - Both geometries present tones at the same frequencies
- Finer mesh on clean regions (wheel and external cavity) shows significant improvement in unsteady quantities (wall pressure and noise)
- The addition of tiny components is less sensitive than grid refinement
- Solving only large components with localized mesh refinement seems to be the most efficient approach

Proper orthogonal decomposition

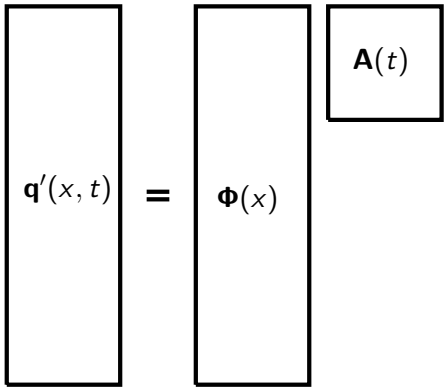
- Reynolds decomposition of volumetric data

$$q'(x,t) = q(x,t) - \bar{q}(x)$$

- Based on singular value decomposition
  - Data-driven, with no physical equations
  - Linear decomposition based on data correlation, matrix $\mathbf{C}(t,t^*)$
  - Space-only matrix $\mathbf{\Phi}(x)$
  - Time-only matrix $\mathbf{A}(t)$

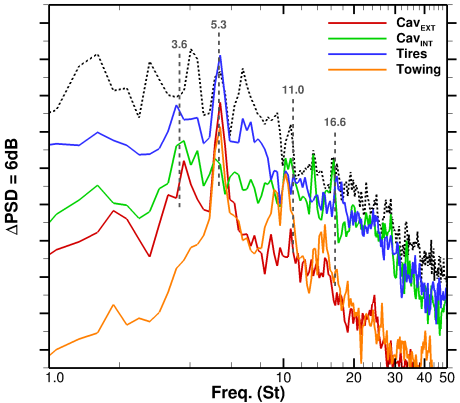
$$\mathbf{C}(t,t^*) = \int_V \mathbf{q}'(x,t)\mathbf{q}'(x,t^*)dV$$

$$\mathbf{q}'(x,t) = \mathbf{\Phi}(x)\mathbf{A}(t)$$

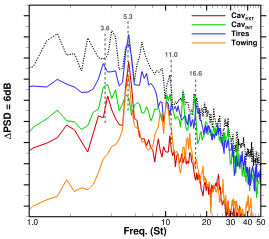


POD - towing link

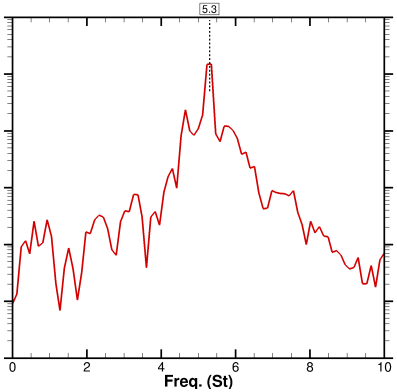
Identification of tonal noise from partial integration using solid FWH surface



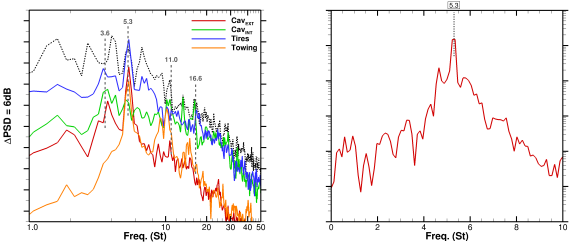
POD - towing link



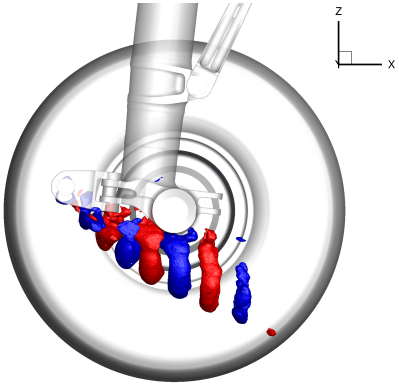
Fourier transform of POD temporal modes $\mathbf{A}(t)$ shows tonal peak at the same frequency from the noise radiation



POD - towing link

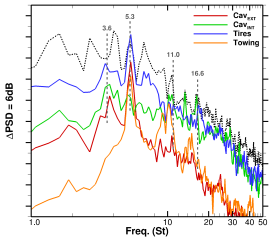


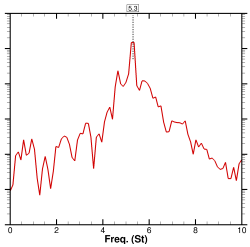
Spatial modes $\phi(\mathbf{x})$ show vortex shedding from towing link and fluid-structure interaction



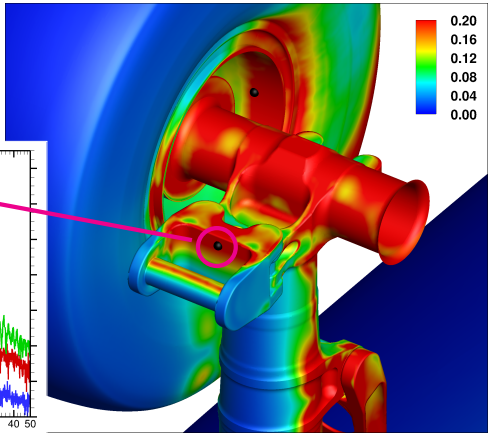
$St_D = f\ D_{wheel}/U_\infty = 5.3$
$St_{tow} = f\ D_{tow}/U_\infty = 0.22$
(typical of cylinder flows)

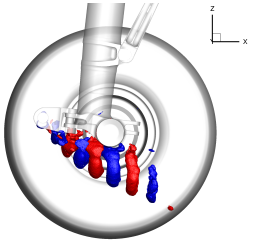
POD - towing link

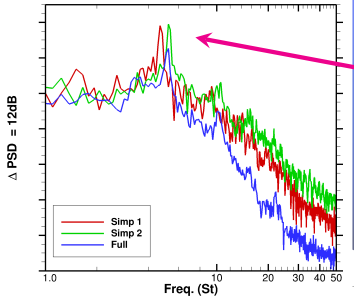




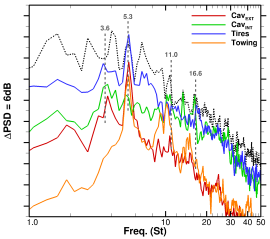
Intense pressure fluctuations on component downstream from the towing link cylinder

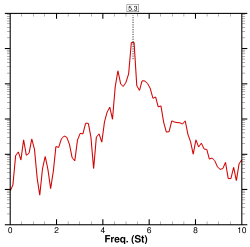


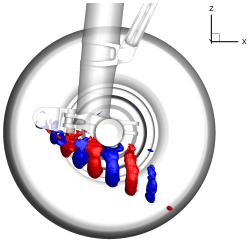


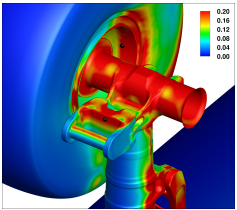


POD - towing link

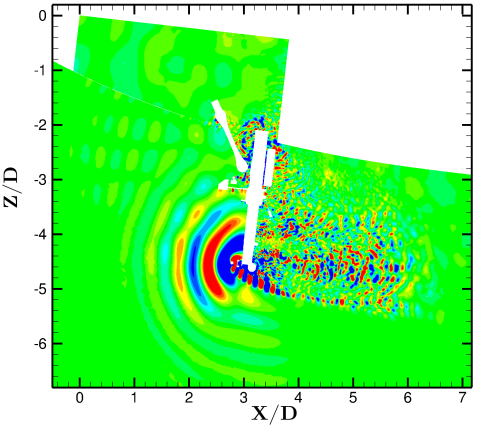






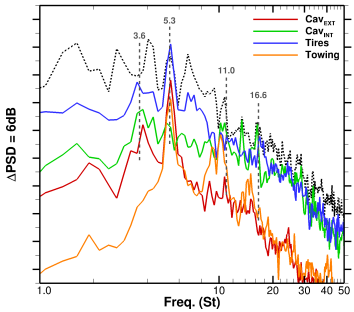


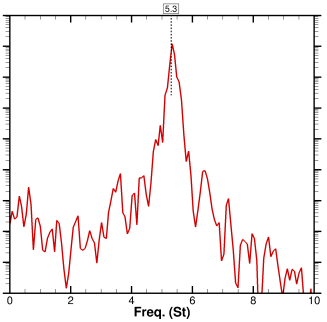
Intense acoustic radiation at the tonal frequency is observed along the symmetry plane



POD - wheel external cavity

- POD analysis of the external cavity of the wheel
  - Coherent structures along the shear-layer
  - Same frequency from the most prominent tone observed at far-field noise





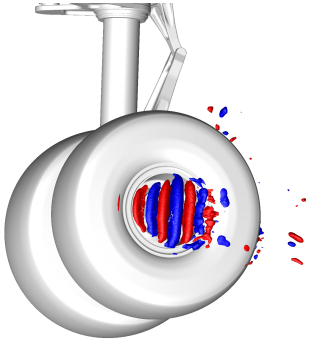


Fig. 39: Temporal and spatial modes from POD analysis of wheel's external cavity.

POD - wheel external cavity

- POD analysis of the external cavity of the wheel
- Rossiter equation for cavities
  - n is n-th Rossiter mode
  - α is an empyrical constant related to phase delay
  - κ is an empyrical constant related to U_c/U_∞

$$St = \frac{n-\alpha}{M_\infty + 1/\kappa}\frac{D}{2R_e} = 5.3$$

$$n = n_h + n_a = 3 + 1$$

$$\alpha = 0.25$$

$$\kappa = 0.65$$

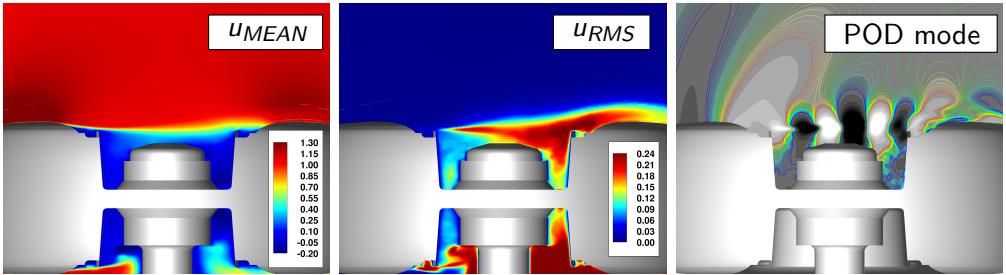


Fig. 39: Flow statistics on the wheel's external cavity.

Cavity modes on wheels

Cavity number	Modes	m=0	m=1	m=2
1 - External	l=1, n=0	**11.0**	**5.3**	**8.9**
	l=2, n=0	20.3	**15.4**	19.4
2 - External	l=1, n=0	25.1	**3.6**	7.1
	l=2, n=0	49.9	**25.3**	26.2
	l=1, n=1	28.5	14.0	**15.3**

Cavity number	Modes	m=0	m=1	m=2
3 - Internal	l=1, n=0	25.1	**3.6**	7.1
	l=2, n=0	49.9	**25.3**	26.2
	l=1, n=1	30.3	17.3	**18.4**
4 - Internal	l=1, n=0	**16.6**	**4.1**	8.0
	l=2, n=0	32.7	17.2	19.1

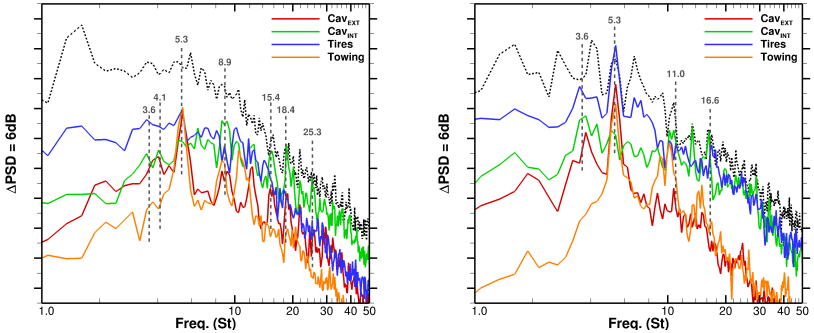
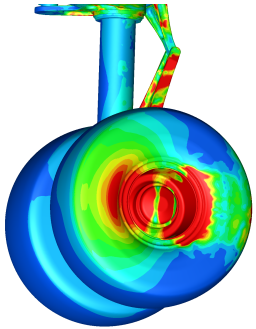


Fig. 40: Noise spectra measured at 90 deg. show multiple tones attributed to both cavities.

Cavity modes on wheels

Cavity number	Modes	m=0	m=1	m=2
1 - External	l=1, n=0	**11.0**	**5.3**	**8.9**
	l=2, n=0	20.3	**15.4**	19.4
2 - External	l=1, n=0	25.1	**3.6**	7.1
	l=2, n=0	49.9	**25.3**	26.2
	l=1, n=1	28.5	14.0	**15.3**

Cavity number	Modes	m=0	m=1	m=2
3 - Internal	l=1, n=0	25.1	**3.6**	7.1
	l=2, n=0	49.9	**25.3**	26.2
	l=1, n=1	30.3	17.3	**18.4**
4 - Internal	l=1, n=0	**16.6**	**4.1**	8.0
	l=2, n=0	32.7	17.2	19.1



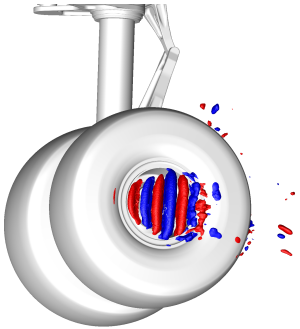


Fig. 40: Excitation of geometrical cavity modes by coherent structures along the shear layer.

POD - fuselage cavity

- Multiple tonal peaks radiate from the fuselage cavity up to St 10
- Cavity is the dominating noise source at low-frequencies considering all components

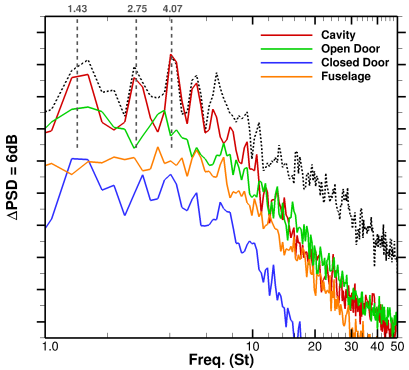


Fig. 41: Component-wise noise prediction at sideline.

POD - fuselage cavity

- Multiple tonal peaks radiates from the fuselage cavity up to St 10
- Cavity is the dominating noise source at low-frequencies considering all components
- Proper orthogonal decomposition identifies 3 (pairs of) modes at the tonal frequencies from the cavity noise spectrum

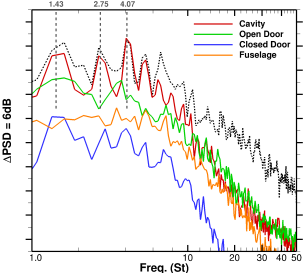


Fig. 41: Component-wise noise prediction at sideline.

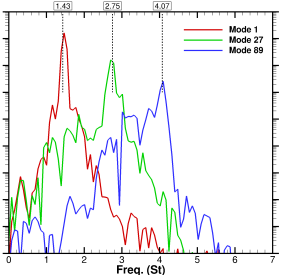


Fig. 42: Spectra of POD temporal modes $\mathbf{A}(t)$.

POD - fuselage cavity

- Multiple tonal peaks radiates from the fuselage cavity up to St 10
- Cavity is the dominating noise source at low-frequencies considering all components
- Proper orthogonal decomposition identifies 3 (pairs of) modes at the tonal frequencies from the cavity noise spectrum

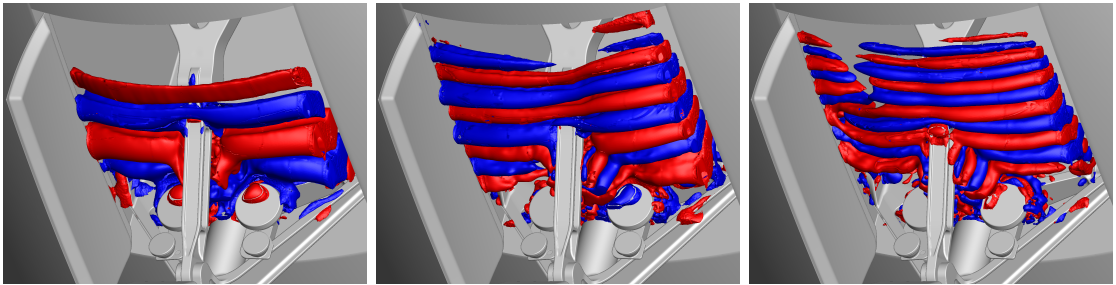


Fig. 41: Spatial modes from POD are related to shear-layer instabilities.

Noise source identification

- Components with tonal noise identified by partial integration of FWH solid surface
- Tones are related to coherent structures within the flow, hence, modal decomposition tools are a must
- Identification of coherent structures in the towing link and cavities
- Devices that break flow coherence can be designed to reduce noise emission levels
- Rossiter feedback mechanism and cavity geometrical modes are important in noise generation

Conclusions

- Numerical simulations of realistic full-scale configurations are feasible
  - DES is required for high Reynolds numbers (modeled wall turbulence)
  - Dual-time stepping (stable large time steps) is required to solve long periods of simulation to obtain convergence of low frequencies (dominate the spectrum)
- Simplification process:
  - Small-scale components can be suppressed for computational savings and easier mesh generation
  - Large-scale components are strictly necessary: these should have been kept inside the fuselage cavity
  - Mesh refinement seems to be more influential than small-scale components
- Lattice-Boltzmann solvers are promissing for this configuration (AIAA 2019-0003)
- Noise source identification by POD can aid the design of noise reduction devices

Acknowledgements

- Drs. Mori Mani, Philippe Spalart and Takao Suzuki for the discussion
- BCFD team for all the support
- Oak Ridge National Laboratory - EOS cluster





Unsteady surface pressure

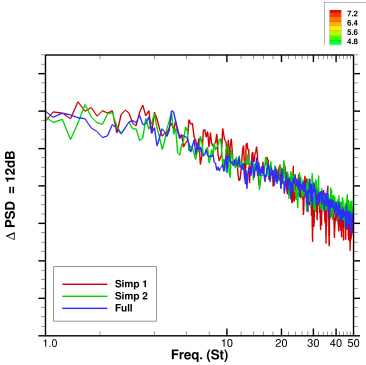


Fig. 43: Wall pressure spectra at the axle.

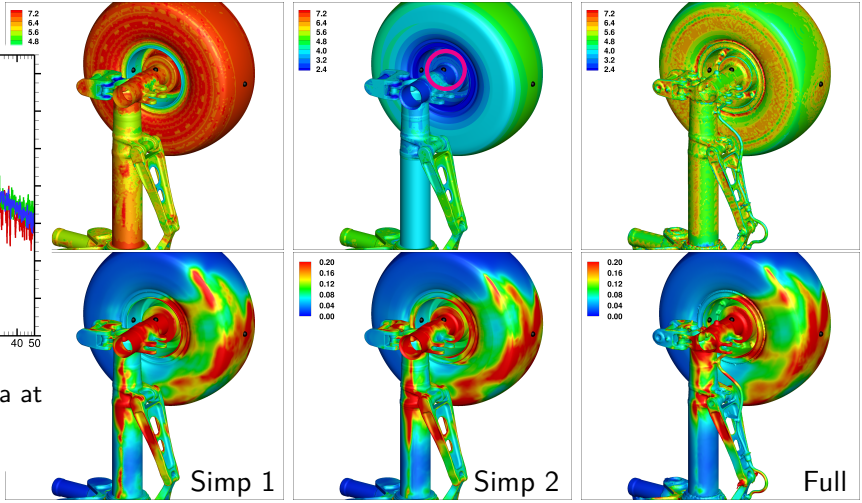


Fig. 42: Mesh resolution and unsteady wall pressure in the wheel-axle region.

Unsteady surface pressure

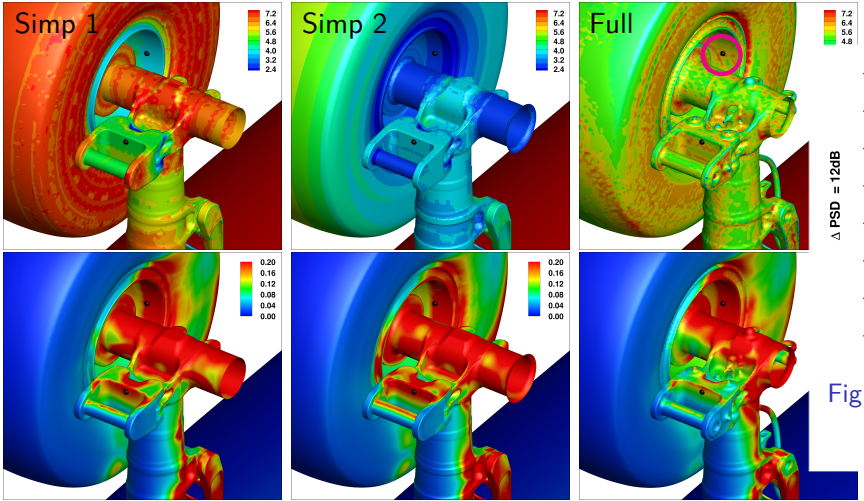


Fig. 44: Mesh resolution and unsteady wall pressure in the wheel-axle region.

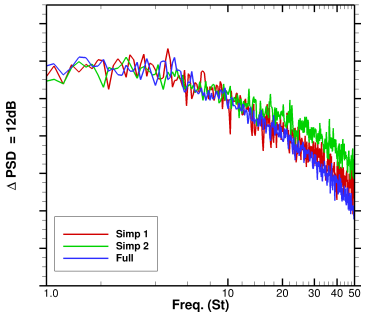


Fig. 45: Wall pressure spectra at the internal cavity.

Solid x permeable surface

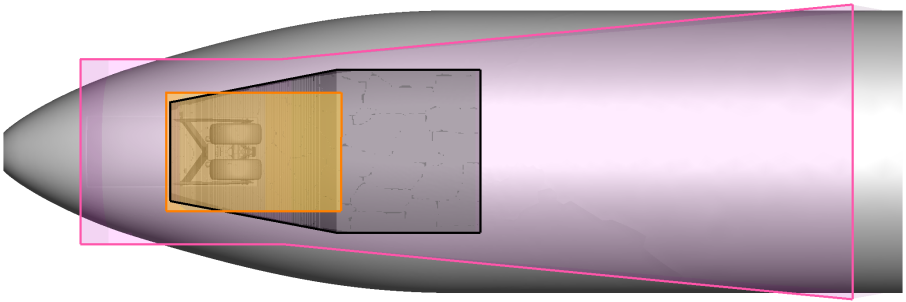


Fig. 46: Permeable surface geometry (top view).

Solid x permeable surface

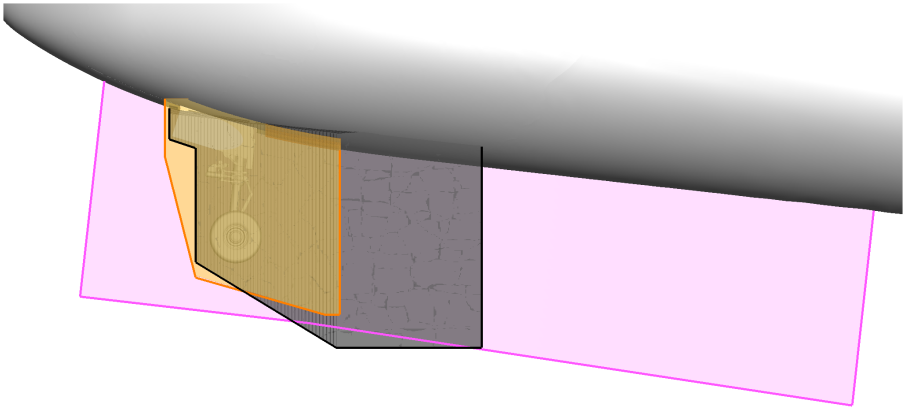
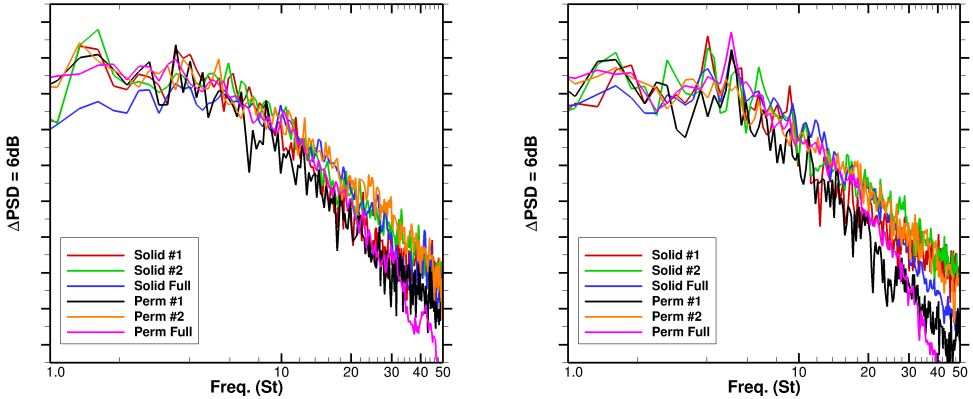


Fig. 47: Permeable surface geometry (side view).

Solid x permeable surface



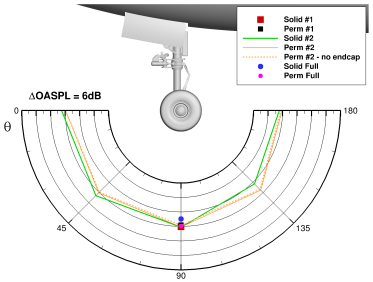
(a) Flyover observer

(b) Sideline observer

Fig. 48: Far-field noise with solid and permeable surfaces.

Permeable surface and endcap

- Endcaps affect mostly the high frequencies for observers at 0 and 180 deg. due to the normal vector orientation
- Noise integration (OASPL) shows good agreements between solid and permeable surfaces at all observers analyzed



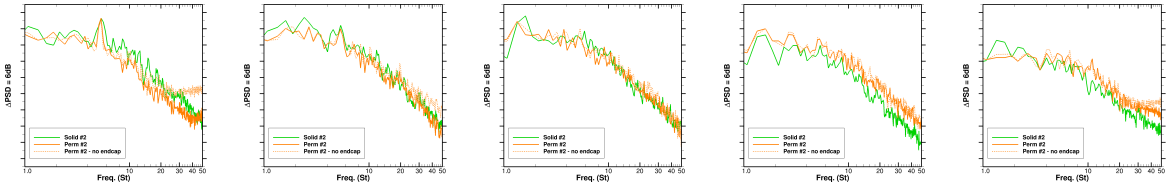


Fig. 49: Noise prediction with endcap technique for multiple observers (symmetry plane).

Wheel cavity division

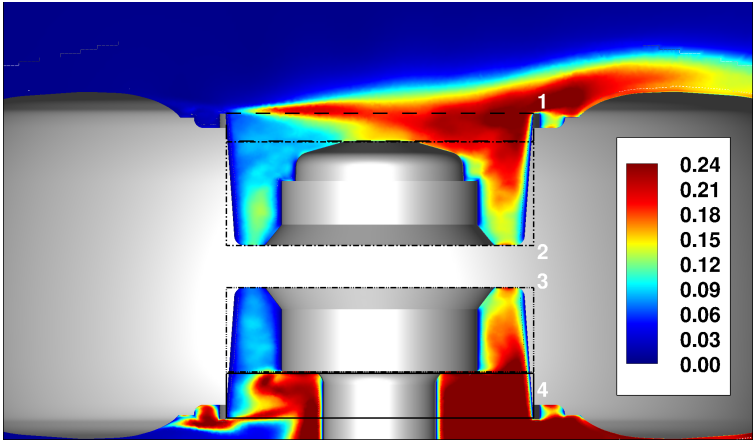
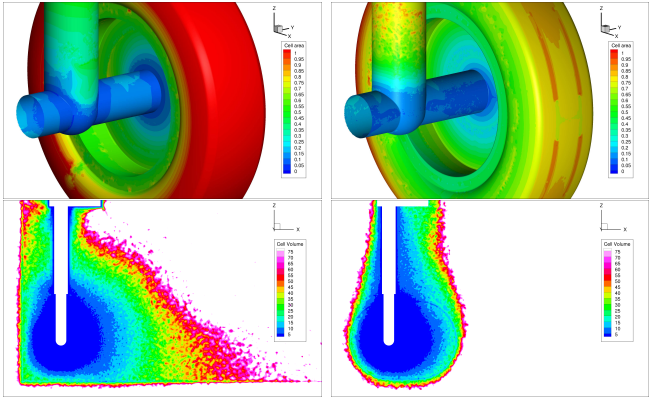


Fig. 50: Sub-cavities considered for the resonance modes.

Mesh topology

- Experiments show that the cavity is the most important region
- First mesh has more elements along the wake
- Second mesh is packed closer to the geometry, with improved results compared to the first grid
- Ricciardi et al., AIAA Journal 2018 56:11, 4379-4399



(a) First mesh (baseline) (b) Second mesh (improved)

Fig. 51: Comparison of numerical and experimental in terms of velocity field for stream-wise component.

Filtered proper orthogonal decomposition

- Reynolds decomposition of volumetric data
- Based on singular value decomposition
- Analysis limited to the wheels cavities

$$\tilde{\mathbf{C}}(t, t^*) = \mathbf{C}(t, t^*) * f$$

$$\mathbf{q}'(x, t) = \mathbf{\Phi}(x)\mathbf{A}(t)$$

$\mathbf{A}(t)$: temporal modes

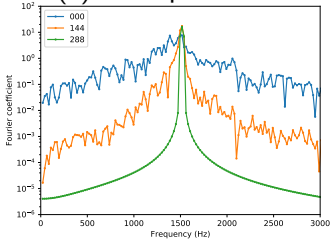


Fig. 52: Fourier transform of modes related to cavity noise (Spectral POD **[9]**).

$\mathbf{\Phi}(x)$: spatial modes

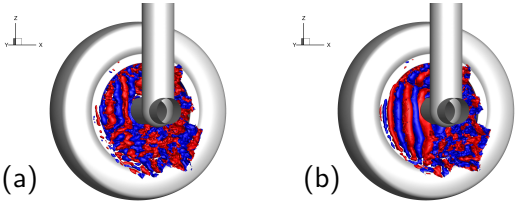


Fig. 53: Coherent structures along the cavity shear layer using (a) unfiltered and (b) filtered POD.

[9] Sieber et al. Journal of Fluid Mechanics, April 2016